Seon, Jean-Antoine; Cenev, Zoran; Zhou, Quan

Automatic Non-Contact Extraction and Independent Manipulation of Magnetic Particles Using Electromagnetic Needle

Document Version
Peer-reviewed accepted author manuscript, also known as Final accepted manuscript or Post-print

Automatic Non-Contact Extraction and Independent Manipulation of Magnetic Particles Using Electromagnetic Needle

Jean-Antoine Seon, Zoran Cenev, and Quan Zhou

Abstract—**Selective and independent manipulation of microparticles is important for a wide range of applications. Compared to other physical principles, magnetic field is promising due to its ability to penetrate most materials and affects only magnetic objects. However, in most non-contact magnetic manipulation systems, all particles in the workspace are moved simultaneously. This paper reports an automatic single-source non-contact magnetic manipulation technique that can selectively extract individual magnetic particles from a population of similar particles and then independently manipulate the extracted particles. We use an electromagnetic needle to create a highly localized magnetic field to achieve the local addressability. The motion of single particles is controlled by adjusting the position of the electromagnetic needle using visual servoing, where two control laws, velocity and position control, have been developed. Experimental results show that a predefined velocity vector can be followed accurately with a directional error of 8.5° and a norm error of 5 μm/s. Similarly, a predefined path can be followed with a position error of 0.5 μm. The capabilities of the proposed method has been demonstrated in four cases: selective extraction of a single particle from a population, separation of two magnetic particles with 11 μm initial gap, independent manipulation of four particles and targeted delivery of two particles onto two separate cells.**

Index Terms—**magnetic devices, motion control, magnetic forces, automation**

I. Introduction

SELECTIVE and independent manipulation of particles is important for many applications, e.g. targeted drug delivery to single cells or particle sorting, where individual particles should be extracted from a population and delivered to different targeted locations. Selective and independent manipulation has been an intrinsic property of techniques such as optical tweezers [1]–[4] and robotic contact manipulation [5], [6]. Optical tweezers have been widely applied in e.g. pattern formation [2] , stiffness characterization of human red blood cells [3], and autonomous manipulation of biological cells [4]. Contact manipulation has also been demonstrated in applications from microassembly [5], [6] to cell injection [7]. However, each technique has its own limitations. For example, optical tweezers relies on the contrast of the refractive index between the targeted particle and the surrounding medium, which limits the types of particles suitable for manipulation.

Contact manipulation requires a delicate force balance between the particle, the tool and the target, which could be challenging in applications [8].

Magnetic manipulation of microparticles has attracted tremendous attention during the past two decades [9]–[12]. This technology is appealing because magnetic field allows non-contact manipulation and affects only magnetic particles with little impact on other objects e.g. cells [9], [10]. Manipulation using magnetic fields has found a wide range of applications such as sorting and trapping of magnetically tagged micro-organisms [12], [13], sub-cellular control of signaling [14] and immunoassays [15], to name a few. A variety of techniques have been developed where the magnetic field is generated by external sources such as permanent magnet [16], electromagnets [17], Helmholtz coils [18] static [19], [20] and dynamic electromagnetic needles [21] or micro-patterned current wires in microfluidic chips [22]. The applied magnetic field can be global, i.e. influencing the whole workspace, or local, i.e. influencing only small part of the workspace where the targeted object resides. A review on recent developments on magnetic manipulation of micro- and nanometer scaled objects can be found in ref. [23].

However, selective and independent manipulation of particles with the presence of other particles is challenging for the current non-contact magnetic manipulation techniques. For most non-contact magnetic manipulation, the magnetic field is global and it influences all particles in the workspace [9], [24]–[28]. These magnetic manipulation technologies work well when manipulating a single magnetic particle or a swarm of particles. To address individual magnetic particles in the presence of other magnetic particles, different methods have been proposed. The difference in material properties of the particles can be exploited to achieve selective manipulation of two or three particles [29]–[31]. The interaction between neighboring magnetic particles can also be utilized to achieve different motion for two particles [32]. Simultaneous manipulation of two particles following two trajectories has also been achieved by generating two independent rotating magnetic fields [33]. Even though those systems can achieve a certain level of independent manipulation, they are hardly able to perform selective extraction. Additionally, the population size is often limited to two to three particles. Independent manipulation can also be achieved by superposition of magnetic fields using specialized surfaces with an array of microcoils [34] or current carrying wires [35]. However, the ability of selective extraction and independent manipulation comes with a cost of

an increasing number of magnetic sources.

In this paper, we report an automatic non-contact magnetic manipulation technique using just a single magnetic source for selective extraction of individual particles from a population and then independently manipulate them. We employ a robotic electromagnetic needle to create a highly localized magnetic field that can move its location across the whole workspace. The highly localized magnetic field exerts localized magnetophoretic forces on a targeted particle. Using visual servoing, we can control the trajectory of a selected particle with little disturbance to neighboring particles. The proposed method has been demonstrated in four cases: selective extraction, separation of two particles, independent manipulation of four particles and targeted delivery of two particles on two separate cells. This work is built upon our previous work on contact manipulation using electromagnetic needle [36].

II. CONCEPT OF THE NON-CONTACT MANIPULATION

To achieve localized non-contact manipulation of magnetic particle, we use a robotic electromagnetic needle (EMN), as shown in Fig. 1a, detailed in Appendix A. A three degrees of freedom nano-positioner is used to control the position of the EMN inside the workspace to manipulate spherical microparticles immersed in deionized water. When a current is supplied to the coil, a highly localized magnetic field gradient is generated, creating a magnetic force[1] $\mathbf{F_m}$ attracting the particle toward the tip of the needle (Fig. 1b). The particle velocity can be adjusted by controlling the motion of the EMN using the nano-positioner (Fig. 1c). Once the particle reaches the desired location, the EMN is demagnetized by applying a decaying electrical signal, canceling the localized magnetic field affecting the particle.

The particles manipulated by the EMN are subject to two different forces: i) the magnetic force, $\mathbf{F_m}$, which is a function of the distance between the particle and the needle tip, and ii) the drag force, $\mathbf{F_d}$, induced by motion in the fluid. These forces can be expressed as follows [36]:

$$\mathbf{F_m} = \frac{2}{3}\pi d_p^3 \rho_p M_p \frac{\beta M_n^2}{(4\beta\delta+1)^3}\underline{\mathbf{u}}_{\mathbf{p-n}}$$
$$\mathbf{F_d} = -3\pi\nu_f d_p \mathbf{v_p} \tag{1}$$

where d_p, ρ_p and M_p are the diameter, density and mass magnetization of the particle respectively, β a coefficient related to the pole shape, M_n the needle core magnetization, δ the distance between the needle tip and the particle, $\underline{\mathbf{u}}_{\mathbf{p-n}}$ the unit vector directing from the particle to the needle tip, ν_f the fluid density and $\mathbf{v_p}$ the particle velocity.

The magnetic field of the EMN is symmetric to the tip of the needle in the half-sphere pointing outwards [36], see Appendix A. Therefore, the eq. 1 is valid for all particles in this half-sphere domain regardless whether a particle is aligned along the EMN axis or not.

[1]In this paper, the following notation is used for the vectors: $\mathbf{F_m} = F_m\underline{\mathbf{F}}_{\mathbf{m}}$ where $\mathbf{F_m}$ represents the total vector, F_m the norm of the vector and $\underline{\mathbf{F}}_{\mathbf{m}}$ the unit vector
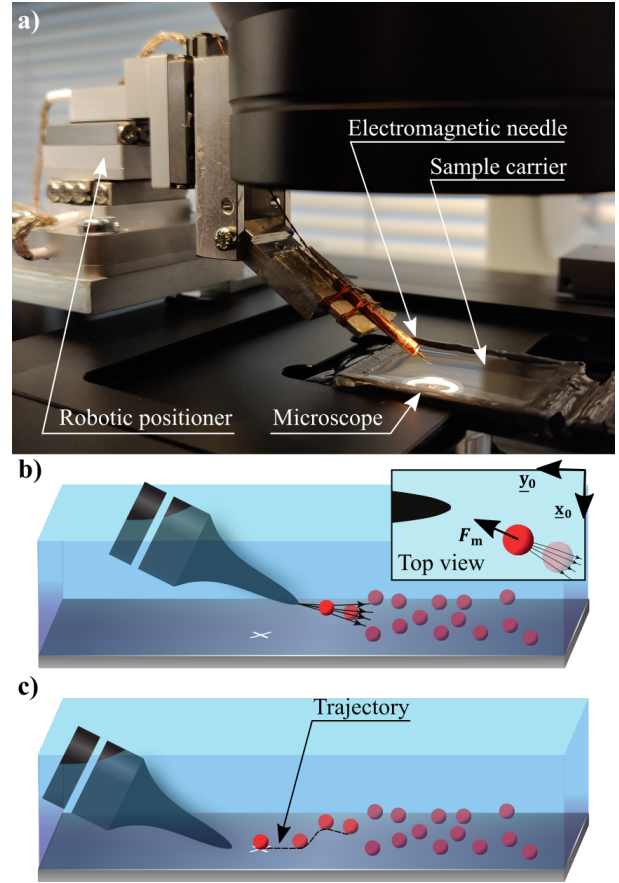

Fig. 1: Concept of selective non-contact magnetic micromanipulation with electromagnetic needle. a) Image of the overall system, b-c) Schematics of automatic non-contact manipulation: b) the EMN creates a field gradient that attract the particle towards the needle tip in a submerged environment; c) by moving the EMN inside the workspace, the position and velocity of the particle can be controlled such that the particle reaches the desired location without contacting the needle tip.

Since the particle size is typically around 5 μm in diameter, the inertia can be neglected. Thus, the motion dynamics, $m\mathbf{a} = \mathbf{F_m} + \mathbf{F_d}$, of a particle subjected to a magnetophoretic force reduces to $-\mathbf{F_d} = \mathbf{F_m}$. Considering that the EMN is placed slightly above the sample carrier during manipulation, the vertical component can be ignored. Thus, the particle dynamics is, in polar coordinates, as follows:

$$v_p = \frac{\alpha}{(4\beta\delta+1)^3}$$
$$\theta_p = atan2(\frac{y_n - y_p}{x_n - x_p}) \tag{2}$$

where v_p is the particle velocity norm, θ_p the angle between the velocity vector $\mathbf{v_p}$ and the x-axis of the reference frame, θ_n the angle between the particle-needle axis and the x axis of the reference frame and $\alpha = 2d_p^2\rho_p M_p\beta M_n^2/9\nu_f$.

As these parameters are difficult to obtain individually, we chose to experimentally estimate the model parameters using the following parametric model:

$$v_p = a\delta^b$$
$$\theta_p = c\theta_n + d \qquad (3)$$

Note that, as the needle tip is not a single point, we used a first order approximation for the relation between the velocity direction and the particle-needle axis.

For microparticle of 5 μm in diameter and a constant current of 0.15 A applied on the EMN, the resulting fit are as follows: $a = 1.967 \times 10^{10}$, $b = -3.311$, $c = 0.7631$ and $d = 0.3642$. More details can be found in Appendix B. It can be noted that the coefficient of the parametric model has a similar order compared to the theory. Based on this model, the particle velocity norm is less than 5 μm/s at a distance of 800 μm when the applied current is 0.15 A. This distance decreases with the applied current.

III. VELOCITY CONTROL

To control the velocity vector, we need to control two variables: the direction and the norm. Therefore, we can consider two cases, a) direction control, and b) norm control.

For direction control, we keep the velocity norm of the particle constant. To adjust the direction to fit the target vector $\mathbf{v_t}$, the controller should move the EMN on a circle centered on the particle position with radius δ being constant (Fig. 2a-I). This can be implemented by using a proportional controller:

$$\mathbf{n} = \mathbf{p} + \delta \begin{bmatrix} cos(\theta_n + \gamma\varepsilon) \\ sin(\theta_n + \gamma\varepsilon) \end{bmatrix} \qquad (4)$$

where ε is the angular error and γ the control gain.

For norm control, the velocity can be adjusted by moving the EMN closer or away from the particle following the particle-EMN vector (Fig. 2a-II). This can be implemented using a proportional-integral controller:

$$\mathbf{n} = \mathbf{n} - \lambda(v_e + \frac{1}{\mu}\sum v_e f_e)\underline{\mathbf{u}}_{\mathbf{p-n}} \qquad (5)$$

where $\mathbf{v_e} = \mathbf{v_t} - \mathbf{v_p}$ is the velocity error, f_e the sampling frequency of the control loop and λ and μ the proportional and integral control gain.

The final control law is simply the sum of the two controllers:

$$\mathbf{n} = \mathbf{p} + \delta \begin{bmatrix} cos(\theta_n + \gamma\varepsilon) \\ sin(\theta_n + \gamma\varepsilon) \end{bmatrix} - \lambda(v_e + \frac{1}{\mu}\sum v_e f_e)\underline{\mathbf{u}}_{\mathbf{p-n}} \qquad (6)$$

The control strategy has been tested in simulation and experiments, in two different scenarios: i) constant norm and variable direction and ii) variable norm and constant direction. In the simulation, the motion of the particle is generated using the data-driven model presented in Section II.

Both simulation and experimental tests use the same control parameters: $\lambda = 0.8$, $\mu = 0.5$, $\gamma = 0.2$ and a sampling frequency $f_e = 20$ Hz. In the simulation, a Gaussian noise of 0.25 μm is added to the particle position to simulate Brownian motion and noisy particle tracking. The particle tracking is done using the ViSP library [37] with a sub-pixel resolution. Details of the experimental setup are described in Appendix A. Video of all the results presented below are also available in the supplementary media file.
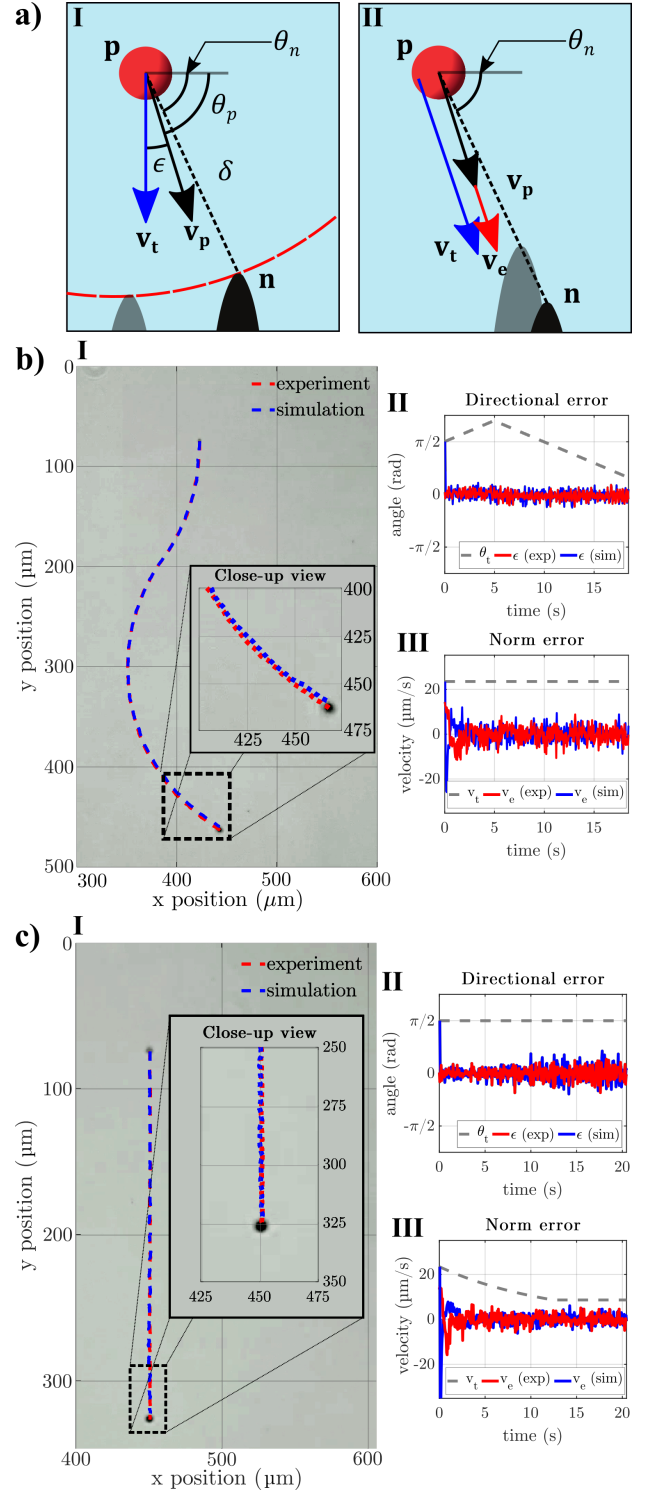
Fig. 2: Velocity control concept and implementation. a) the control strategy: I) direction controller and II) norm controller. Experimental and simulation results of b) time-varying orientation and fixed norm and c) fixed orientation and time-varying norm. Experimental trajectories are represented in red while the simulations are overlaid in blue. b-II and c-II show the error of the direction controller while b-III and c-III show the error of the norm controller. The controller target is represented as a gray dashed line.

A. Constant norm and variable direction

In this experiment, the particle motion is controlled automatically in directions parallel to the substrate plane and towards the EMN. The velocity norm is fixed at 23.5 µm/s while the direction changes linearly from 90° to 126° and to 28°. The test results after 18.45 seconds are shown in Fig. 2b. It can be seen that the velocity vector is controlled to fit the time-varying target vector. Both the directional and norm errors are converging well. The standard deviation of the directional error is 0.12 rad in an experiment and 0.16 rad in a simulation. The standard deviation of the norm errors is also similar at 3.97 µm/s experimentally and 4.12 µm/s in simulation. The final position difference between the simulation and experimental results is only 3.17 µm, showing the precision of the fitted model.

B. Variable norm and constant direction

In this experiment, the particle velocity norm is controlled, varying from 23.4 µm/s to 8.6 µm/s while the velocity direction is kept pointing downward. The test results after 20.5 s are visible in Fig. 2c. In detail, the standard deviation of the directional errors is 0.15 rad and 0.2 rad for the experiment and the simulation respectively. It is interesting to note that, as the velocity norm decreases, the direction error slightly increases. We attribute this to the more dominant Brownian force compared to the magnetic force when the distance between the tip and the particle is large. Additionally, the standard deviation of the norm error is 3.14 µm/s and 4.87 µm/s in experiment and simulation respectively. The final position of the particle in simulation is 2.71 µm different from the position obtained during the experiment.

C. Controller accuracy

Table I summarizes the velocity control results. Experimentally, the mean directional error is always lower than 0.15 rad which is equivalent to 8.5° and the mean norm error is less than one body length per second. The results obtained in the simulation are very close showing that the model has good prediction power for the system.

IV. POSITION CONTROL

We implemented a path following algorithm to evaluate the position control capability of the system. The control algorithm has two layers. The first layer generates the desired velocity vector based on the path input and the current position of the particle. The second layer generates the needle motion to fit the velocity vector generated by the first layer. In practice, the needle motion is generated by the algorithm presented in Section III.

TABLE I: Summary of velocity control errors

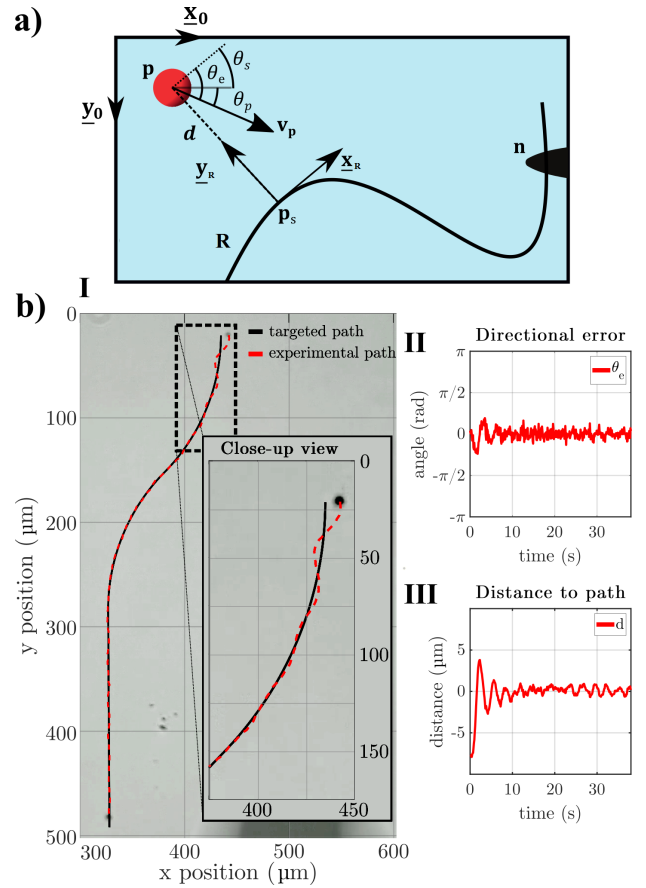|	Rms(ε) rad	Std(ε) rad	Rms(v_e) µm/s	Std(v_e) µm/s
A - Exp	0.12	0.12	3.97	3.97
A - Sim	0.16	0.16	4.34	4.12
B - Exp	0.15	0.15	3.13	3.14
B - Sim	0.2	0.2	4.87	4.87

Fig. 3: Positioning control concept and implementation. a) Illustration of the control strategy. $\mathbf{p}$ (with x_p, y_p) and $\mathbf{n}$ (with x_n, y_n) denote particle and EMN position, respectively. p_s is the orthogonal projection of the particle position on the path $\mathbf{R}$ to be followed. $\underline{\mathbf{x}_R}$ and $\underline{\mathbf{y}_R}$ denote the unit vector which defines the Fernet frame in $\mathbf{p_s}$ (a moving frame attached to the path with $\underline{\mathbf{x}_R}$ being the tangent to the path $\mathbf{R}$). $\mathbf{d}$ is the distance between the path $\mathbf{R}$ and the particle $\mathbf{p}$; θ_e is the angle between the velocity vector of the particle $\mathbf{v_p}$ and the $\underline{\mathbf{x}_R}$. θ_p is the angle between the reference (camera) frame (with $\underline{\mathbf{x}_0}$ and $\underline{\mathbf{y}_0}$) and the velocity vector of the particle $\mathbf{v_p}$, θ_s is the angle between the $\underline{\mathbf{x}_0}$ and $\underline{\mathbf{x}_R}$ unit vectors. b) Experimental results for a path following at constant velocity. The particle trajectory is represented in red while the target path is overlaid in black. b-II and b-III show the control errors.

The desired velocity vector is planned using the control law presented in [38]. The kinematics of the particle can be expressed in a mobile frame attached to the orthogonal projection, $\mathbf{p_s}$, of the particle on the path (Fig. 3). The resulting equations are as follows:

$$\begin{aligned} \dot{s} &= \frac{v_p}{1 - dC(s)}cos(\theta_e) \\ \dot{d} &= v_p sin(\theta_p) \\ \dot{\theta}_e &= \omega - \dot{s}C(s) \end{aligned} \quad (7)$$

where $\omega = \dot{\theta}_p$ is the rotational velocity of the particle motion vector, s the curvilinear abscissa on the path, $C(s)$ the

curvature of the path, d the distance with the path and θ_e is the angle between the particle velocity vector and the tangent vector to the path in $\mathbf{p_s}$.

This system can be transformed into a chained system using a change of variables (the complete derivation can be found in [38]). Then, proportional state feedback which ensures convergence of the distance and the orientation errors can be achieved:

$$u = -\dot{s}\phi_1 d - |\dot{s}|\phi_2(1-dC(s))tan(\theta_e) \qquad (8)$$

where u is a control variable, and ϕ_1 and ϕ_2 are two positive gains.

The control variable u is linked to the rotational velocity ω, which updates the velocity vector at each iteration [38]:

$$\omega = \frac{u + (\dot{d}C(s) + d\frac{\partial C(s)}{\partial s})tan(\theta_e)}{(1-dC(s))(1+tan^2(\theta_e))} + \dot{s}C(s) \qquad (9)$$

This path-following strategy has been implemented on the experimental setup and has been tested with the following parameters: ϕ_1=0.2 and ϕ_2=0.4. The velocity vector is servoed using the same parameters presented in the previous section. The velocity norm of the particle is fixed to 11.75 µm/s and both controllers run at the same frequency (10 Hz). The particle is placed with an initial position error of 7.6 µm and its trajectory is visible in Fig. 3b-I. This initial error is used to show the convergence of the controller. The position error decreases before it stabilizes (Fig. 3b-III) with a standard deviation of 1.53 µm. Similar behavior is observed for the orientation error (Fig. 3b-II). When the particle reaches the path, the mean position error decreases to 0.46 µm, which is less than 10% of the particle size. This shows that accurate position control with sub-micrometer precision can be achieved.

V. SELECTIVE EXTRACTION

The selective property of the EMN has been evaluated experimentally. A lower current (0.012 A) is used to reduce the magnetic field and to make it more localized around the needle tip (see Appendix B for the characterization of the motion induced by lower currents). The particle motion is controlled using the velocity controller. In these experiments, the user selects a target point in the field of view of the camera and the controller servos the velocity of a particle to reach the targets at a constant speed of 9.4 µm/s (V-A) or 7 µm/s (V-B). Once the target is reached, the current provided to the EMN is switch to zero, then the needle is removed. Due to the lower current, the gains used for velocity control were changed to $\lambda = 0.25$, $\mu = 2$ and $\gamma = 0.08$ for eq. 6. Two experiments are reported in this section: i) extraction of a particle from a population, ii) separation of two magnetic particles. See the supplementary multimedia file for videos.

A. Extraction from a population

To demonstrate selective extraction, we move a single particle (no. 6 in Fig. 4a) to a new location with 9 visible adjacent particles (hundreds of particles are present in the sample carrier). Initially, the minimum distance between particle 6
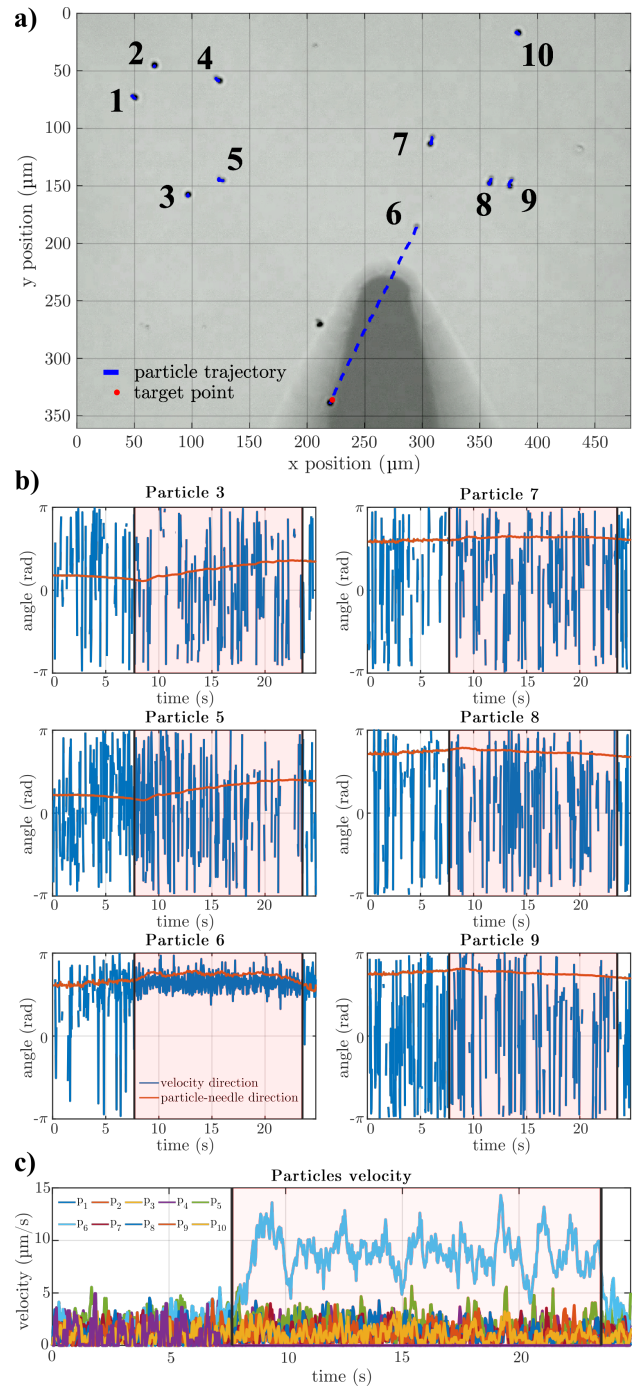

Fig. 4: Selective manipulation. a) Trajectories after 24.8 s. Particle 6 is moved to the target point (red dot). The initial configuration is represented as transparent. b) Evolution of the particle velocity vector (blue) and the particle-EMN vector (red) for the closest particles (3, 5, 6, 7, 8 and 9). When the particle is affected by the magnetophoretic force, these two values are close to each other. Discontinuities are visible when the particle is not moving. The red background corresponds to the period when the EMN is active. c) Evolution of the particles' velocity during the experiment. Mean velocity of ~3 µm/s is equivalent to the Brownian motion.

and the rest of the population is 64 μm. The position of the particle 6 after 16.5 s of manipulation is 213 μm away from the nearest visible particle. From Fig. 4a, we also notice that other particles besides particle 6 are little disturbed during the 16.5 s long experiment. Fig. 4b compares the direction of the velocity vector of each particle and the direction of the particle-EMN vector with respect to the horizontal axis of the reference (camera) frame. These two values are correlated for particle 6 showing that the particle is attracted by the needle. For the rest of the population, little correlation is observed, showing that other particles are not disturbed by the magnetophoretic force. Additionally, the velocities norm of those particles is around 3 μm/s, similar to the velocity norm induced by the Brownian motion (Fig. 4c).

When the particle reaches the positioning threshold, i.e. <2 μm, the controller is turned off. Then the needle is removed creating a disturbance to the particle. The final positioning error is 3.0 μm. It can be noted that once the EMN is turned off, the velocity of particle 6 quickly decreases from 10 μm/s to less than 5 μm/s, which is similar to the velocity of the other particles (Fig. 4c).

B. Separation of two particles

In this experiment, two particles are initially spaced by 10.6 μm (Fig. 5a). The goal is to extract particle 2 with little disturbance to particle 1. When the EMN is turned on (at 3.5 s in Fig. 5b), both particles are moved in towards the EMN. However, the magnetophoretic force decreases quickly with the increasing distance between the particles. After 10 s, the direction of motion for particle 1 stops being correlated with the particle-EMN vector, showing that the magnetophoretic force becomes negligible.

The close-up view in Fig. 5a further illustrates the trajectory of particle 1. The blue line represents the 0-10s trajectory, and the red line represents the 10-30s trajectory. The blue trajectory follows the same direction as particle 2, but the red trajectory clearly shows the randomness caused by Brownian motion.

When particle 1 stops being attracted by the EMN (10-th second), the distance between the two particles is 35 μm and the distance between particle 1 and the EMN is 83 μm (Fig. 5c). At this distance, and according to our model (see Appendix B), the velocity of the particle is equivalent to the velocity induced by Brownian motion. Thus, for input current of 0.012 A the effective radius of the EMN is around 83 μm. Additionally, the distance between the two particles increases linearly from 10.6 μm to 183 μm (Fig. 5d).

VI. INDEPENDENT MANIPULATION

The highly localized magnetic field of the EMN allows independent manipulation of multiple particles successively. Two experiments are reported in this section: independent manipulation of i) four particles in deionized water and ii) two particles in cell culture. The results reported below were obtained using the same control gain as the one used in Section V. Similarly, the user manually selects the target point of each particle and the velocity norm is servoed to either 11.7 μm/s (VI-A) or 7 μm/s (VI-B).
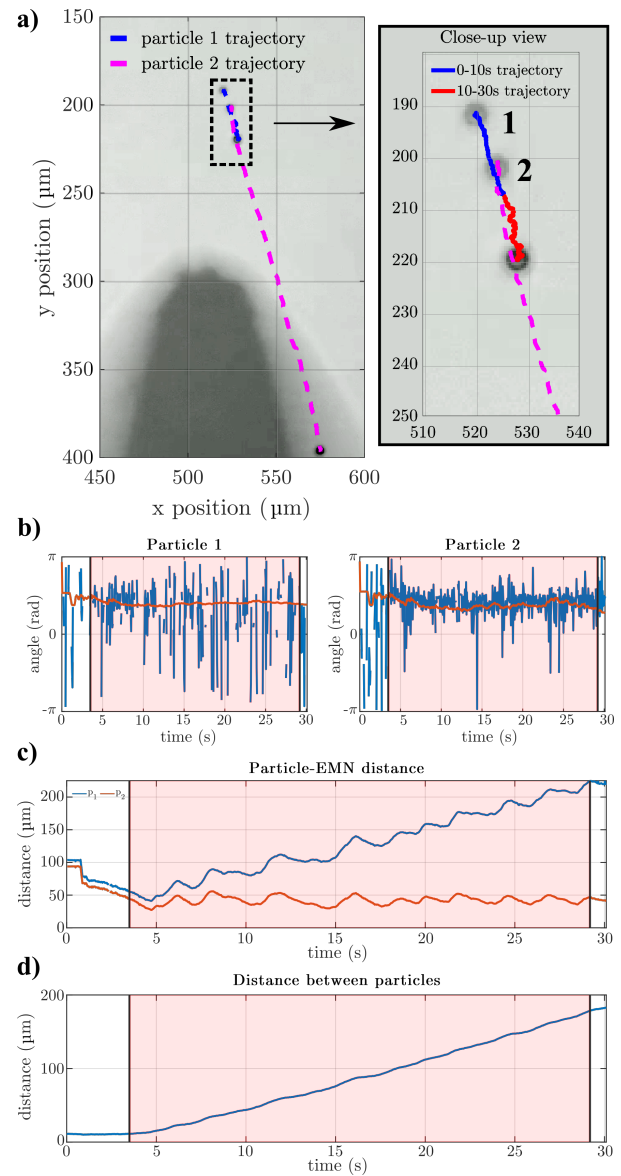

Fig. 5: Separation of two magnetic particles. a) Trajectories after 30 s of manipulation. The initial configuration is represented as transparent. The inset represents the trajectory of the particle 1 divided into two colors (blue and red). b) Evolution of the particle velocity vector (blue) and the particle-EMN vector (red) for the two particles. c) Evolution of the distance between the two particles and the EMN. d) Evolution of the distance between the two particles.

A. Independent manipulation of four particles

In this experiment, a group of four particles is in a random configuration such that the distance between two particles ranges from 105 μm to 258 μm (Fig. 6a). The control algorithm successively controls the motion of each particle. Fig. 6a shows the motion of the different particles during the whole manipulation experiment. While manipulating each particle, the other particles are slightly moved from their position due to the Brownian motion and the hydrodynamic forces. When particle 1 is manipulated for a duration of

40 seconds, the other three particles are displaced by about 15 μm from their initial position. Small displacements are also observed during the manipulation of the other particles: 10 μm for particle 2, 12 μm for particle 3 and 6 μm for particle 4. Each particle is positioned accurately during its manipulation with a positioning error of less than 5 μm. However, their positions deviate when manipulating other particles due to hydrodynamic forces. The final positioning error is 23 μm (∼6%) for particle 1, 16 μm (∼4%) for particle 2, 8 μm (∼2%) for particle 3 and 3.2 μm (∼1%) for particle 4. The distances between the four particles and their respective targets are illustrated in Fig. 6b.

Figure 6c depicts the instantaneous velocity of each particle during the whole manipulation. The figure shows that the mean velocity of the three particles not under manipulation is around 3 μm/s, equivalent to the velocity induced by the Brownian motion (see Appendix B). Thus, the manipulation is independent where only one particle is manipulated at a time.

B. Independent manipulation of particles within a cell culture

This last experiment shows the potential of our manipulation technique for biological application. We demonstrate particle delivery to targeted cells within a cell culture. Initially, the particles are dispensed in the cell culture (see Appendix A for more details). Two particles hovering on the substrate are selectively positioned onto two different cells. Particle 1 is approached by the EMN and guided to a targeted position on a cell, denoted with red dot in Fig. 7a. In a similar fashion, particle 2 is guided to a targeted position near another cell. The two particles are successively manipulated without disturbing the position of the other (Fig. 7a). Once the controller switches to manipulate particle 2, the position error of particle 1 is 0.78 μm, blue line in Fig. 7b. At the end of the manipulation, the error remains about the same, i.e. 0.73 μm. However, this behavior is not observed for particle 2. When the controller is turned off, the position error for particle 2 is 1.3 μm, however, this value increased up to 5.4 μm at the end of the experiment, red line in Fig. 7b. One possible interpretation is that the adhesion between particle 1 and the cell is greater than the Brownian force whereas particle 2 failed to create a firm contact with the cell and thus it drifted away after switching off the controller.

VII. DISCUSSION

A. Performance analysis

To quantitatively and qualitatively evaluate the performance of our manipulation technique in respect to the state-of-the-art automatic non-contact magnetic manipulation systems, we selected the following indicators: particle size, number of selectively manipulated microparticles, population size, population disturbance (beyond Brownian motion), minimum distance between manipulated particles, type of magnetic field, controller accuracy and degrees of freedom of the particle. The summary is shown in Table II.

It is interesting to note that only [35], [31] and [9] show manipulation results for objects smaller than 10 μm. All the other manipulation setups are designed to work with objects
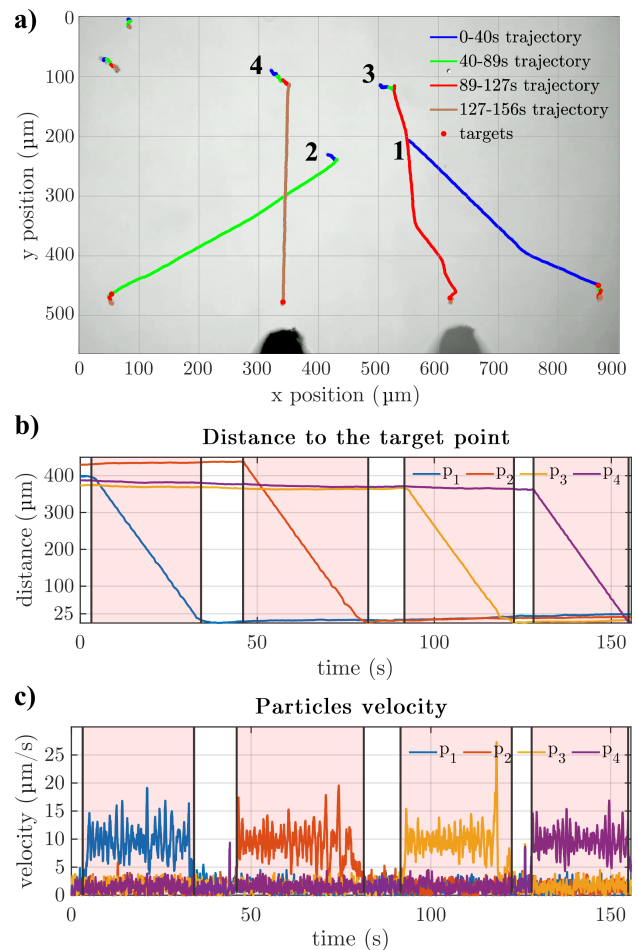

Fig. 6: Independent manipulation of four particles. a) Trajectories after 156 s. Four particles are moved to four different targets (black dot). Each color corresponds to the trajectories of the particles when one of the four targeted particles is manipulated. b) Evolution of the distance between the four particles and their respective targets. The red areas correspond to the period when the EMN and the controller are active. c) Evolution of the velocity of each particle during the manipulation. The mean velocity of ∼3 μm/s is equivalent to the Brownian motion velocity.

at least 20 times bigger. The experiments reported in [20], [29], [30], [39], and [33] exhibit a population limited to 3 particles distanced at few millimeters and the scaling comes at a great cost in control accuracy and selectivity. In [35], a population of 6 particles is reported. However, the population is largely disturbed during the performance of the selective experiments due to the design of the setup. Our approach allows manipulating particles with multiple neighbors (up to 10 visible particles in Section V.A) separated by a small distance (∼10 μm in Section V.B).

Even if all these manipulation setups allow to manipulate single particles, their selectivity is poor because of the utilization of global magnetic fields. Only [20] demonstrates true selective manipulation but it requires the particles to be outside the radius of influence of the magnetic source which is around 500 μm. The selectivity reported in [35] is limited due to

TABLE II: Comparison between magnetic-based non-contact automatic manipulation setups able to perform selective and/or independent manipulation

| Ref	Particle size	Number of manipulated particles	Population size	Population disturbance	Minimum distance	Type of magnetic field	Degrees of freedom
[20]	100 µm (sphere)	3	3	No (if distance > 500 µm)	>5 mm	Localized	Full plane
[29]	1.5×4.9 mm^2	2	2	Yes	>10 mm	Global	Full plane
[30]	600×300 μm^2	3	3	Yes	>5 mm	Global	Full plane
[31]	4.5 µm (sphere)	3	3	Yes	> 50 µm	Global	Full plane
[32]	250-500 µm (sphere)	2	2	Yes	> 1 mm	Global	Full plane
[33]	5.6×1.5 mm^2	2	2	Yes	31.8 mm	Global	Full plane
[35]	5-8 µm (sphere)	3	2-6 (visible)	Yes	24 µm	Global + Localized	Full plane
This work	5 µm (sphere)	4	2-10 (visible)	No (if distance > 85 µm)	10.6 µm	Localized	Half plane
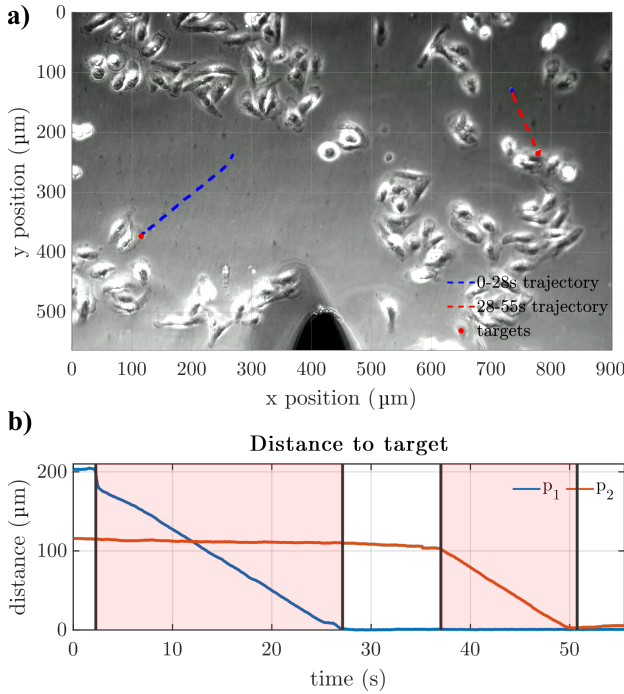
Fig. 7: Independent positioning of two particles on cells. a) Trajectories of the two particles during the manipulation. Trajectories are in blue for particle 1 and in red for particle 2. The two targets are in red. The initial configuration is represented as transparent. b) Evolution of distance between each particle and its respective target. The red areas represent the period when the EMN and the controller are active.

its fixed positioning in the workspace. Our system exhibits a flexible radius of influence, e.g. 85 µm for 12 mA and 150 µm for 30 mA (Appendix B, Fig. 8b) that allows to selectively manipulate particle anywhere in the workspace.

The main limitation of our approach compared to other magnetic manipulation setup is the lack of motion control in every direction. The current system only allows to control motion in the direction of the needle tip (attractive motion). Two solutions can be considered to solve this problem: i) adding a second EMN opposite to the existing one to create a symmetrical system or ii) put the needle in the vertical position.

B. Comment on selectivity

The proposed approach can selectively manipulate the particles that are close to the electromagnetic needle. The particles in the middle of a population can be manipulated if there is a path between the particles larger than the effective range of the EMN. Alternatively, the particles surrounding the targeted particle can be manipulated first to open a path (see the manipulation of particle 3 during the experiment in section V.A). In practice, when the particle population is homogeneous (e.g. in biological application), successively targeting the particles on the periphery of the population is a reasonable solution.

The selectivity of the proposed approach can be adjusted by changing the current used in the coil. A lower current creates a more focused magnetic field allowing to perform manipulation with better selectivity, whereas a higher current enables higher manipulation speed and greater range. The actual current should be selected depending on the application. Additionally, different mediums also affect the selectivity of the system as the viscosity impacts the dynamics of the particles. For a fixed distance and current, the velocity of the particle will be lower in a medium with high viscosity, meaning that our system will be even more selective.

VIII. SUMMARY

In this paper, we reported an automatic non-contact motion control technique based on an electromagnetic needle for selective extraction and independent manipulation of magnetic particles. The needle generates a magnetic field gradient localized in the vicinity of the tip. The magnetophoretic force created by this gradient allows the particle close to the needle to be attracted to the EMN tip. Then, the motion of the particles is controlled by adjusting the position of the electromagnetic needle using a nano-positioner.

This automatic non-contact manipulation approach has been validated in simulation and experimentally using velocity and position control. The particle motion was controlled using visual servoing and the developed controllers have shown an accuracy of around 8.5° and 4 μm/s for the velocity control and around 0.5 µm for the position control. Selective extraction has

also been demonstrated where two adjacent particles ($\sim 10\,\mu m$) can be separated. Moreover, we have shown independent manipulation of up to four particles as well as independent positioning of two microparticles onto cells.

The next step of this work includes application in biological studies such as precise drug delivery onto individual biological cells. In addition, a second electromagnetic needle will be added to enhance the controllability and dexterity such that particles can be moved in any direction within the workspace.

APPENDIX A
SYSTEM DESCRIPTION

A stainless-steel wire with a thickness of 0.5 mm and a sharp tip of $\sim 30\,\mu m$ was coiled with copper wire in 4 layers, each layer is ~ 25 mm long, yielding around 300 coil turns. The needle was fastened to an aluminum holder and tightened by another copper wire and Teflon string (Fig. 1a). The holder was screwed to an aluminum adapter mounted on a 3-DOF robotic nanopositioner (SLC1720, SmarAct). The whole device was attached to an aluminum adapter connected to an inverted microscope (Axio Vert.A1, Zeiss).

The robotic nanopositioner was controlled by a control unit (MCS-3D, SmarAct) and each axis has an accuracy of tens of nanometers and a maximum velocity higher than 20 mm/s. The current supplied to the electromagnetic needle was generated by an AD/DA converter (NI 6343, National Instruments) connected to a personal computer. The current to the coil was amplified by a linear amplifier (TS200, Accel Instruments). A 3.3 μF capacitor was connected in parallel to the coil.

Similarly as in [36], the magnetic field from the EMN is localized at the tip and spreads radially as shown in Fig. 8a (numerical simulation performed in Comsol Multiphisics 5.3). The maximum field at the needle tip is 60 mT at a current of 0.15 A (Fig. 8b).

The manipulation experiments were performed in a confined well with an open top, modified from a two-chamber glass slide. Superparamagnetic microparticles (1–10 μL of stock dispersion, particle concentration: 0.001–0.1 g.L–1) were add to 50–100 μL of water (deionized Milli-Q). A dose of $\sim 2\,\mu L$ solution yields hundreds of microparticles within the sample carrier.

During control experiments, images and video acquisition were performed using a Grasshopper GS3-U3-23S6M-C camera. The scene was observed with an X20 objective. The camera resolution is 1920 pixels $\times$ 1200 pixels and the resulting field-of-view is about 902 μm $\times$ 564 μm. Experiments were performed at 20 frames per second for velocity control and 10 frames per second for positioning control.

Accurate control of the needle was obtained by calibrating the nano-positioner with respect to the camera. The homography matrix between the camera frame and the actuator frame ($^c p =^c H_a \times^a p$) was computed by moving and tracking the needle tip in the field of view of the camera while recording the positions of all motion stages of the nano-positioner.

The microparticles used for experiments are polystyrene encapsulated iron-III-oxide $Fe_3O_4@PS$ (from Microparticles
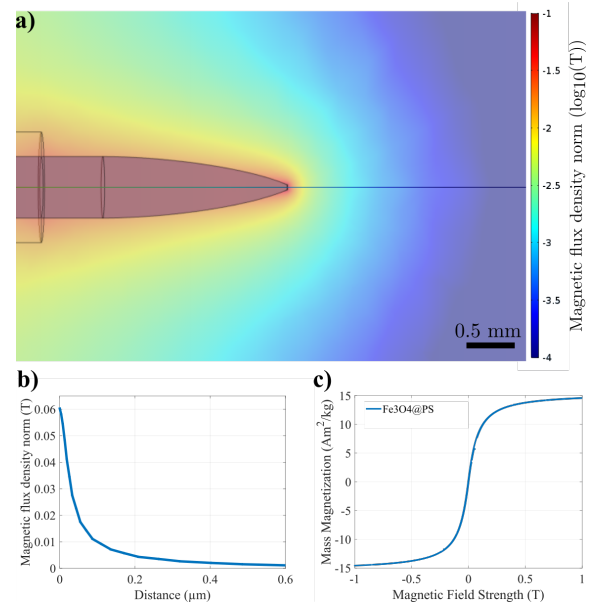

Fig. 8: Magnetic characteristics of the EMN setup. a) Logarithmic 2D map of the magnetic field (Numerical Simulation of the magnetic field intensity created by the EMN for a supplied current of 0.15 A). b) Magnetic field (magnetic flux density) along the axis of the EMN. c) The mass magnetization of a microparticle used for experiments.

GmbH, Germany) with a diameter of 4.5 μm. Figure 8c shows the magnetization curves of these particles.

10000 MDA-MB-231 breast carcinoma cells were seeded in a round petri dish (10 mm diameter) and allowed to attach overnight. After removal of the cell culture medium (Roswell Park Memorial Institute, RPMI) supplemented with 1% penicillin, 1% non-essential amino acids, 1% L-glutamine, 10% foetal bovine serum, the cells were washed once with fresh 1X PBS buffer (pH 7.4) and fixed using 4% paraformaldehyde (PFA) for 15 min at 37°C. Afterwards, the cells were washed twice with the PBS buffer and suspended in the PBS. The medium was finally changed to soapy water.

APPENDIX B
MODEL VALIDATION

The model has been validated by gathering distance-velocity vectors experimentally. Data were acquired by fixing the position of the EMN and supplying a constant current in the coil while recording the motion of multiple particles (see attached video file). Particles used during these experiments are $Fe_3O_4@PS$ (see Appendix A). The image acquisition was performed at 5000 frames per second using a High-Speed Camera (Phantom v2012).

After each experiment, particles were tracked to compute their instantaneous velocity. Then, functions were fitted to find the relation between the velocity norm $\mathbf{v_p}$ (μm/s), and the distance to the needle tip δ (μm), as well as the relation between the velocity angle θ_p (rad) and the particle-needle axis angle θ_n.

Trajectories of hundreds of particles were recorded to model the velocity fields created by the needle. Fig. 9a and b compare
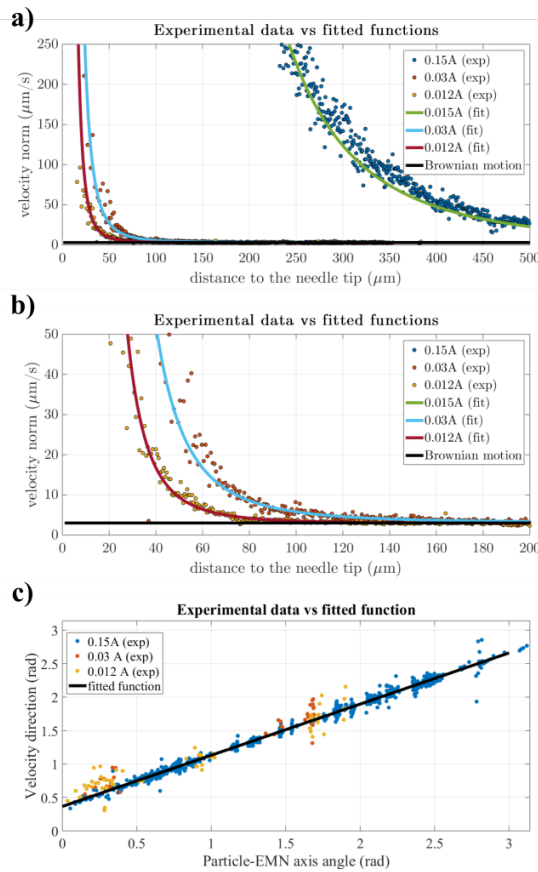
a)

b)

c)

Fig. 9: Comparison of experimental data and fitted model for velocity norm and direction, and different current value. a) Fitted function for the velocity norm for three different current values (0.15, 0.03 and 0.012 A). b) Close view for the lower current. c) Fitted function for the velocity direction.

the measured particle velocity norm with the fitted functions for different current supplied to the coil (0.15, 0.03 and 0.012 A). All the data were fitted using a function of the form $v_p = a\delta^b + c$. The results are visible in Table III. We attribute the c coefficient mostly to the Brownian motion. The fitted function is very close to the theoretical model as the coefficients are of the same order (b∼-3). Moreover, Brownian motion was modeled by observing particles moving freely in the workspace. The average recorded motion was 3.3 μm/s (with a standard deviation of 1 μm/s), which is similar to the value of the coefficient c in the fitted models. Note that all the identified models are valid for a needle-particle distance up to 550 μm, which is the maximum distance that can be observed using an x20 magnification objective.

The effective range of the EMN was deducted from these models: 85 μm for 0.012A, 150 μm for 0.03A and more than 800 μm for 0.15A.

The direction of the velocity vector is not a function of the current and the fitted function is: $\theta_p = a\theta_n + b$ with a=0.7631 and b=0.3642. Coefficient a is not one due to the relatively large size of the needle compared to the size of the particle. The goodness of this fit is $R^2 = 0.92$. The fitted function, as well as the measured direction, are visible in Fig. 9c.

TABLE III: Coefficients of velocity norm and distance relation

| Current (A)	a	b	c	R^2
0.15	1.967×10^{10}	-3.311	0	0.79
0.03	5.811×10^6	-3.166	3.077	0.91
0.012	3.707×10^6	-3.387	2.884	0.90

REFERENCES

[1] A. Ashkin, "Acceleration and Trapping of Particles by Radiation Pressure," *Physical Review Letters*, vol. 24, no. 4, pp. 156–159, 1 1970. [Online]. Available: https://link.aps.org/doi/10.1103/PhysRevLett.24.156

[2] J. E. Curtis, B. A. Koss, and D. G. Grier, "Dynamic holographic optical tweezers," *Optics Communications*, vol. 207, no. 1-6, pp. 169–175, 2002.

[3] M. M. Brandao, A. Fontes, M. L. Barjas-Castro, L. C. Barbosa, F. F. Costa, C. L. Cesar, and S. T. O. Saad, "Optical tweezers for measuring red blood cell elasticity: application to the study of drug response in sickle cell disease," *European Journal of Haematology*, vol. 70, no. 4, pp. 207–211, 4 2003. [Online]. Available: http://doi.wiley.com/10.1034/j.1600-0609.2003.00027.x

[4] A. Banerjee, S. Chowdhury, and S. K. Gupta, "Optical Tweezers: Autonomous robots for the manipulation of biological cells," *IEEE Robotics and Automation Magazine*, vol. 21, no. 3, pp. 81–88, 2014.

[5] V. Sariola, M. Jääskeläinen, and Q. Zhou, "Hybrid microassembly combining robotics and water droplet self-alignment," *IEEE Transactions on Robotics*, vol. 26, no. 6, pp. 965–977, 2010.

[6] D. J. Cappelleri, Z. Fu, and M. Fatovic, "Caging for 2D and 3D micromanipulation," *Journal of Micro-Nano Mechatronics*, vol. 7, no. 4, pp. 115–129, 2012.

[7] Y. Sun and B. J. Nelson, "Biological cell injection using an autonomous microrobotic system," *The International Journal of Robotics Research*, vol. 21, no. 10-11, pp. 861–868, 2002.

[8] Q. Zhou and V. Sariola, "Unified View of Robotic Microhandling and Self-Assembly," in *Robotic Microassembly*.   Wiley Online Library, 2010, pp. 107–143.

[9] X. Wang, C. Ho, Y. Tsatskis, J. Law, Z. Zhang, M. Zhu, C. Dai, F. Wang, M. Tan, S. Hopyan, H. McNeill, and Y. Sun, "NANOROBOTS: Intracellular manipulation and measurement with multipole magnetic tweezers," *Science Robotics*, vol. 4, no. 28, 2019.

[10] S. Schuerle, I. A. Vizcarra, J. Moeller, M. S. Sakar, B. Özkale, A. M. Lindo, F. Mushtaq, I. Schoen, S. Pané, V. Vogel, and B. J. Nelson, "Robotically controlled microprey to resolve initial attack modes preceding phagocytosis," *Science Robotics*, vol. 2, no. 2, p. eaah6094, 1 2017. [Online]. Available: http://robotics.sciencemag.org/lookup/doi/10.1126/scirobotics.aah6094

[11] S. Martel and M. Mohammadi, "Using a swarm of self-propelled natural microrobots in the form of flagellated bacteria to perform complex micro-assembly tasks," *Proceedings - IEEE International Conference on Robotics and Automation*, pp. 500–505, 2010.

[12] H. Lee, A. M. Purdon, V. Chu, and R. M. Westervelt, "Controlled assembly of magnetic nanoparticles from magnetotactic bacteria using microelectromagnets arrays," *Nano Letters*, vol. 4, no. 5, pp. 995–998, 2004.

[13] B. B. Yellen, R. M. Erb, H. S. Son, R. Hewlin, H. Shang, and G. U. Lee, "Traveling wave magnetophoresis for high resolution chip based separations," *Lab on a Chip*, vol. 7, no. 12, pp. 1681–1688, 2007.

[14] F. Etoc, D. Lisse, Y. Bellaiche, J. Piehler, M. Coppey, and M. Dahan, "Subcellular control of Rac-GTPase signalling by magnetogenetic manipulation inside living cells," *Nature Nanotechnology*, vol. 8, no. 3, pp. 193–198, 3 2013. [Online]. Available: http://dx.doi.org/10.1038/nnano.2013.23http://www.nature.com/articles/nnano.2013.23

[15] K. S. Kim and J.-K. Park, "Magnetic force-based multiplexed immunoassay using superparamagnetic nanoparticles in microfluidic channel." *Lab on a chip*, vol. 5, no. 6, pp. 657–664, 2005.

[16] P. Ryan and E. Diller, "Magnetic actuation for full dexterity microrobotic control using rotating permanent magnets," *IEEE Transactions on Robotics*, vol. 33, no. 6, pp. 1398–1409, 2017.

[17] R. Pieters, H. W. Tung, S. Charreyron, D. F. Sargent, and B. J. Nelson, "RodBot: A rolling microrobot for micromanipulation," *Proceedings - IEEE International Conference on Robotics and Automation*, vol. 2015-June, no. June, pp. 4042–4047, 2015.

[18] A. Snezhko and I. S. Aranson, "Magnetic manipulation of self-assembled colloidal asters," *Nature Materials*, vol. 10, no. 9, pp. 698–703, 9 2011. [Online]. Available: http://dx.doi.org/10.1038/nmat3083http://www.nature.com/articles/nmat3083

[19] Z. Zhang, F. Long, and C. H. Menq, "Three-dimensional visual servo control of a magnetically propelled microscopic bead," *IEEE Transactions on Robotics*, vol. 29, no. 2, pp. 373–382, 2013.

[20] H. H. See, S. C. Herath, Y. Du, H. Asada, and P. C. Chen, "Localized Manipulation of Magnetic Particles in an Ensemble," *IEEE Access*, vol. 6, pp. 24075–24088, 2018.

[21] B. D. Matthews, D. A. LaVan, D. R. Overby, J. Karavitis, and D. E. Ingber, "Electromagnetic needles with submicron pole tip radii for nanomanipulation of biomolecules and living cells," *Applied Physics Letters*, vol. 85, no. 14, pp. 2968–2970, 10 2004.

[22] C. P. Gooneratne, O. Yassine, I. Giouroudi, and J. Kosel, "Selective manipulation of superparamagnetic beads by a magnetic microchip," *IEEE Transactions on Magnetics*, vol. 49, no. 7, pp. 3418–3421, 2013.

[23] Q. Cao, Q. Fan, Q. Chen, C. Liu, X. Han, and L. Li, "Recent advances in manipulation of micro- and nano-objects with magnetic fields at small scales," *Materials Horizons*, 2019.

[24] J. Yu and L. Zhang, "Reversible swelling and shrinking of paramagnetic nanoparticle swarms in biofluids with high ionic strength," *IEEE/ASME Transactions on Mechatronics*, vol. 24, no. 1, pp. 154–163, 2019.

[25] F. Long, D. Matsuura, and C. H. Menq, "Actively Controlled Hexapole Electromagnetic Actuating System Enabling 3-D Force Manipulation in Aqueous Solutions," *IEEE/ASME Transactions on Mechatronics*, vol. 21, no. 3, pp. 1540–1551, 2016.

[26] M. P. Kummer, J. J. Abbott, B. E. Kratochvil, R. Borer, A. Sengul, and B. J. Nelson, "Octomag: An electromagnetic system for 5-DOF wireless micromanipulation," *IEEE Transactions on Robotics*, vol. 26, no. 6, pp. 1006–1017, 2010.

[27] S. Chowdhury, W. Jing, and D. J. Cappelleri, "Controlling multiple microrobots: recent progress and future challenges," *Journal of Micro-Bio Robotics*, vol. 10, no. 1-4, pp. 1–11, 2015.

[28] J. Yu, B. Wang, X. Du, Q. Wang, and L. Zhang, "Ultra-extensible ribbon-like magnetic microswarm," *Nature Communications*, vol. 9, no. 1, p. 3260, 12 2018.

[29] J. Zhang, P. Jain, and E. Diller, "Independent control of two millimeter-scale soft-bodied magnetic robotic swimmers," *Proceedings - IEEE International Conference on Robotics and Automation*, vol. 2016-June, pp. 1933–1938, 2016.

[30] E. Diller, S. Floyd, C. Pawashe, and M. Sitti, "Control of multiple heterogeneous magnetic microrobots in two dimensions on nonspecialized surfaces," *IEEE Transactions on Robotics*, vol. 28, no. 1, pp. 172–182, 2012.

[31] S. Das, E. B. Steager, M. A. Hsieh, K. J. Stebe, and V. Kumar, "Experiments and open-loop control of multiple catalytic microrobots," *Journal of Micro-Bio Robotics*, vol. 14, no. 1-2, pp. 25–34, 2018.

[32] M. Salehizadeh and E. Diller, "Two-agent formation control of magnetic microrobots in two dimensions," *Journal of Micro-Bio Robotics*, vol. 12, no. 1-4, pp. 9–19, 2017.

[33] N. D. Nelson and J. J. Abbott, "Generating two independent rotating magnetic fields with a single magnetic dipole for the propulsion of untethered magnetic devices," *Proceedings - IEEE International Conference on Robotics and Automation*, vol. 2015-June, no. June, pp. 4056–4061, 2015.

[34] D. Cappelleri, D. Efthymiou, A. Goswami, N. Vitoroulis, and M. Zavlanos, "Towards mobile microrobot swarms for additive micromanufacturing," *International Journal of Advanced Robotic Systems*, vol. 11, 2014.

[35] E. Steager, D. Wong, J. Wang, S. Arora, and V. Kumar, "Control of multiple microrobots with multiscale magnetic field superposition," *International Conference on Manipulation, Automation and Robotics at Small Scales, MARSS 2017 - Proceedings*, pp. 1–6, 2017.

[36] Z. Cenev, H. Zhang, V. Sariola, A. Rahikkala, D. Liu, H. Santos, and Q. Zhou, "Manipulating Superparamagnetic Microparticles with an Electromagnetic Needle," *Advanced Materials Technologies*, vol. 3, no. 1, 2018.

[37] E. Marchand, F. Spindler, and F. Chaumette, "ViSP for visual servoing: a generic software platform with a wide class of robot control skills," *IEEE Robotics & Automation Magazine*, vol. 12, no. 4, pp. 40–52, 12 2005. [Online]. Available: http://ieeexplore.ieee.org/document/1577023/

[38] J. A. Seon, B. Tamadazte, and N. Andreff, "Decoupling Path Following and Velocity Profile in Vision-Guided Laser Steering," *IEEE Transactions on Robotics*, vol. 31, no. 2, pp. 280–289, 2015.

[39] M. Salehizadeh, S. Salmanipour, J. Zhang, and E. Diller, "Controlling Multiple Microrobots using Homogeneous Magnetic Fields," *IEEE Conference on Robotics and Automation*, 2018.

Jean-Antoine Seon recieved the Ph.D. degree in Automation and Robotics from the University of Bourgogne Franche-Comté (Besançon, France) in 2017 and a Master degree in mechatronics and micro-systems from ENSMM (Besançon, France) in 2014. In 2017, he joined the robotic instruments group at School of Electrical Engineering, Aalto University, Finland. His research interests are currently focused on optimal planning and control for both contact and contact-less micromanipulators.
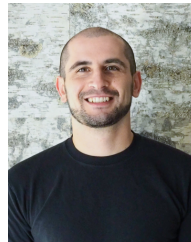
Zoran Cenev received his B.Sc. degree in Mechatronics from Saints Cyril and Methodius University, Skopje, Macedonia in 2011 and his M.Sc. degree in Mechatronics and Micromachines from Tampere University of Technology, Tampere, Finland in 2014. He is currently a PhD candidate in micro- and nano robotics at Aalto University, Espoo, Finland. His work and interests are focused in magnetic-based micromanipulation, droplet microrobotics, and particle micromanipulation at air-liquid interfaces.

Quan Zhou received the M.Sc and Dr. Tech. degrees from Tampere University of Technology, Finland. He is currently an Associate Professor leading the Robotic Instruments Group at School of Electrical Engineering, Aalto University, Finland. He was a Professor at Northwest Polytechnical University, Xi'An, China. His main research interests are micro- and nano manipulation and automation methods. His work has been published in major international journals including Nature Communications, Physical Review Letters, Advanced Materials, Small and IEEE Transactions on Robotics. Prof. Zhou was the winner of the Anton Paar Research Award for Instrumental Analytics and Characterization. He was also the general chair of International Conference on Manipulation, Automation and Robotics at Small Scales, MARSS 2019. Prof. Zhou was the coordinator of EU FP7 project FAB2ASM, the first PPP project of the European Economic Recovery Plan. He was also the chair of IEEE Finland Joint Chapter of Control System Society, Robotics and Automation Society and System Man and Cybernetics Society.